

IHVIN-GAT-Based Path Planning for Parallel and Independent Manipulation of Heterogeneous Microtargets via OETs in Unstructured Environments

Jiaxin Liu, Shilong Qin^{ID}, Qing Shi^{ID}, Senior Member, IEEE, Juan Cui^{ID}, Hen-Wei Huang, Qiang Huang^{ID}, Fellow, IEEE, Toshio Fukuda^{ID}, Life Fellow, IEEE, and Huaping Wang^{ID}, Member, IEEE

Abstract—Manipulating heterogeneous microtargets based on optoelectronic tweezers (OETs) to construct micropatterns with specific distribution and ordered arrangement enables recapitulating the spatial architecture of cells in native tissues, and has significant potential in tissue regeneration, medical diagnostics, and cell behavior research. However, the uncertain disturbances in liquid environment, collision risk, and electrokinetic interference in OETs system can cause microtargets to deviate from the safe and controlled state, especially for manipulation tasks with heterogeneous microtargets. Here, we propose an improved hierarchical value iteration network (IHVIN)-GAT-based path planning method for parallel manipulation of heterogeneous microtargets with independent control, integrating goal assignment, feature extraction, and decentralized decision-making. The Kuhn-Munkres-based goal assignment model periodically modifies the matching relationship between microtargets and goal positions to reduce the task complexity. High-order features involving path planning are extracted by an IHVIN model, and then selectively aggregated and convolved through GAT to yield real-time locomotion strategies for all microtargets. For the issues of constraint variability

Manuscript received 26 February 2024; revised 1 July 2024; accepted 19 August 2024. This work was supported in part by the National Key Research and Development Program of China under Grant 2023YFB4705400; in part by the National Natural Science Foundation of China under Grant 62073042, Grant 62222305, and Grant U22A2064; in part by the Beijing Natural Science Foundation under Grant 4232055; in part by the Science and Technology Innovation Program of Beijing Institute of Technology under Grant 2022CX01019; and in part by the Fundamental Research Funds for the Central Universities. This article was recommended by Associate Editor H. Pan. (Corresponding author: Huaping Wang.)

Jiaxin Liu and Shilong Qin are with the Key Laboratory of Biomimetic Robots and Systems, Beijing Institute of Technology, Ministry of Education, Beijing 100081, China (e-mail: 3120205097@bit.edu.cn; qinsl12345@163.com).

Qing Shi, Qiang Huang, and Huaping Wang are with the Intelligent Robotics Institute, School of Mechatronical Engineering, Beijing Institute of Technology, Beijing 100081, China (e-mail: shiqing@bit.edu.cn; qhuang@bit.edu.cn; wanghuaping@bit.edu.cn).

Juan Cui is with the State Key Laboratory for Manufacturing Systems Engineering, Xi'an Jiaotong University, Xi'an 710049, China (e-mail: cuijuan@nuc.edu.cn).

Hen-Wei Huang is with the School of Electrical & Electronic Engineering, Nanyang Technological University, Singapore 20001 (e-mail: henwei.huang@ntu.edu.sg).

Toshio Fukuda is with the Department of Micro-Nano Systems Engineering, Nagoya University, Nagoya 464-8603, Aichi, Japan (e-mail: tofukuda@nifty.com).

Color versions of one or more figures in this article are available at <https://doi.org/10.1109/TSMC.2024.3449132>.

Digital Object Identifier 10.1109/TSMC.2024.3449132

and system heterogeneity, discrete locomotion constraints are developed through analysis of escape mechanism, then embedded into modeling procedures and converted to heterogeneous edge weights in graph domain. The simulation and experimental results demonstrate the desired performance of the IHVIN-GAT model in high timeliness, high strategy quality, and compatibility for microtarget number, where up to 20 microtargets from three categories are parallel manipulated within 16 s to form arbitrary micropatterns recapitulating microscale architecture of cells in native tissues. We anticipate that our method will contribute to construct more biomimetic microstructures with heterogeneous cells for biomedical applications in the future.

Index Terms—Automation at the microscale, graph attention network (GAT), optoelectronic tweezers (OETs) control, robotic micromanipulation.

I. INTRODUCTION

AS THE basic units to represent life activity, cells are self-aggregated in specific distribution and ordered arrangement to construct tissues and organs with intricate structure and biofunction in vivo [1]. Spatial positions of multiple types of cells regulate cell-cell interactions [2] (e.g., secretion and transmission of signaling molecules), which in turn influencing cell behaviors and gene expression. To recapitulate this biological feature [3] *in vitro*, microaggregates with predefined spatial architecture are formed by accurate transport, arrangement, and immobilization of heterogeneous microtargets in high-throughput, which is called micropatterning. Micropatterning [4] is promising in fabricating biofunctional cellular models for cell behavior research [5], tissue regeneration [6], [7], and medical diagnostics [8]. Contact manipulation methods [9], [10] with end-effectors, including micropipette, microprobe, and microgripper can achieve spatial arrangement and accurately controlling microtarget position by the pick-and-place strategy. Nonetheless, the number of end-effectors limits manipulation efficiency to sequential level. Field-driven manipulation methods (e.g., acoustic tweezers [11], [12] and magnetic tweezers [13], [14], [15]) enable actuating microtargets in clusters to form micropatterns by modulated physical field. However, these methods are deficient in independent control of individual microtarget due to the identical response of

microtargets under the same external excitation [16]. Involving architectural integrity with large-scale heterogeneous microtargets and accurate position control, micropatterning tasks has urgent and significant demands on both high efficiency and single-target-level precision [17].

With high throughput and dexterity [18], [19], optoelectronic tweezers (OETs) have great potential for fulfilling the increasing demands on efficiency and single-target-level precision [20]. By projecting optical patterns on adjacent photosensitive-coated area [21], exclusive virtual electrode with a local electric field for each microtarget is generated, which enables simultaneous trapping and differential actuation [22]. However, current OETs-based manipulation methods generally remain at manual sequential operation level [23], or just being customized with preprogrammed schemes [24], which regulate the response of cellular clusters on-demand, but is deficient in single-target-level precision. Several crucial issues hinder the development of OET-based parallel micromanipulation with independent control. In unstructured liquid environment, microtargets lacking environmental perception ability are susceptible to collision with other controlled targets or impurities with random distribution and dynamic movement. Furthermore, the locomotion of microtargets will be disturbed by electrokinetic effects from adjacent virtual electrodes and other microtargets, which even results in escape of microtargets from virtual electrode's trap. Additionally, the electrokinetic interference from microtargets with differentiated electrical characteristics is inconsistent, which indicates unexpected escape accidents are inevitable without intricate constraints for manipulation tasks with heterogeneous microtargets. Due to scale effects and unclear mechanical models, the escape mechanism in scenarios with multitargets interaction has not yet been addressed, nor have the quantitative analysis methods for escape boundary conditions. Consequently, it is necessary to develop an OETs-based parallel manipulation method with independent control, that enables locomotion decision making for multiple microtargets from different types, while avoiding collisions and escape risks caused by electrokinetic interference.

Several decision-making strategies for multitargets at microscale have been studied with utilizing traditional multiagent pathfinding (MAPF) algorithms, such as partially observable Markov decision process (POMDP) [25], [26], PRM* [27], D* Lite [28], etc. At macroscale, the adaptability and performance of multiagent path-planning are facilitated by developing appropriate heuristic functions [29], optimization functions, and algorithm structures [30], [31]. However, computational time exponentially proliferates as the number of microtargets increases, resulting in non-negligible decision-making delay, which hinders in-time replanning under dynamic interference and emergency risks in unstructured liquid environment. Furthermore, modeling all microtargets as consistent agents ignores the system heterogeneity for manipulation tasks with heterogeneous microtargets, which result in unsafe or cost-prohibitive trajectories. Actually, currently reported path planning experiments at microscale, whether based on OETs or optical tweezers, only limited to a few cellular microtargets (about 3 or 4) from one category.

By offloading the expensive computation costs to off-line training procedures [32], [33], deep reinforcement learning methods [34], [35], [36], [37] provide decentralized path planning solutions with high timeliness, and illustrates considerable performance in heterogeneous multirobot systems [38]. Nevertheless, these algorithms exhibit limited efficacy in addressing multitarget decision-making tasks with an indeterminate number of agents [39], and thus lack sufficient compatibility for manipulation tasks with diverse number of microtargets. In contrast to fixed entity boundary of agent at macroscale, both physical collision and electrokinetic interference regulate the safe radius of microtargets, which changes with surrounding environments instead of remaining constant. With time-varying safe radius as constraints, collision-free and escape-free locomotion cannot be guaranteed. Therefore, a real-time path planning method for multitargets decision making is on demand, which integrates compatibility for microtarget's numbers as well as strategies for the system heterogeneity and constraint variability.

In this article, a learning-based decision-making method based on an improved hierarchical value iteration network (IHVIN)-GAT path planning network for parallel manipulation tasks with heterogeneous microtargets is proposed by integrating goal assignment, feature extraction, and decentralized decision-making. Goal assignment based on the Kuhn–Munkres algorithm is performed periodically for all microtargets within category, thereby the matching scheme of microtargets and goal positions is dynamically modified, while decoupling the entire task according to the microtarget's category. To extract high-ordered features associated with path planning, an IHVIN with a parallel architecture to learn local environment and long-term goal-directed information is designed. Subsequently, decentralized decision-making is achieved by selectively aggregating and convoluting high-order features based on the attention mechanism in graph attention network (GAT), yielding real-time locomotion actions for all microtargets. Simulation results demonstrate the overall performance of the IHVIN-GAT model in terms of high timeliness, high strategy quality, and compatibility of microtarget number. The feasibility of the decision-making approach is verified by manipulating up to 20 microtargets from three categories for arbitrary micropatterning, which recapitulates the microscale architecture of cells in native tissues (such as hepatic lobules and vascular walls). This approach is promising for the biomedical tasks with demands on high efficiency and single-target-level precision, including micropatterning. The primary contributions of this study are as follows.

- 1) For the issues of system heterogeneity and constraint variability, we analyze the escape mechanism to develop the discrete locomotion constraints in the OETs system. The discrete constraints are embedded into modeling procedures and converted to heterogeneous edge weights in graph domain, thus enhancing the attention mechanism in the GAT model.
- 2) The IHVIN network is proposed with a parallel architecture to facilitate extracting high-order features from both local environment and long-term goal-directed information, and even outperforms the

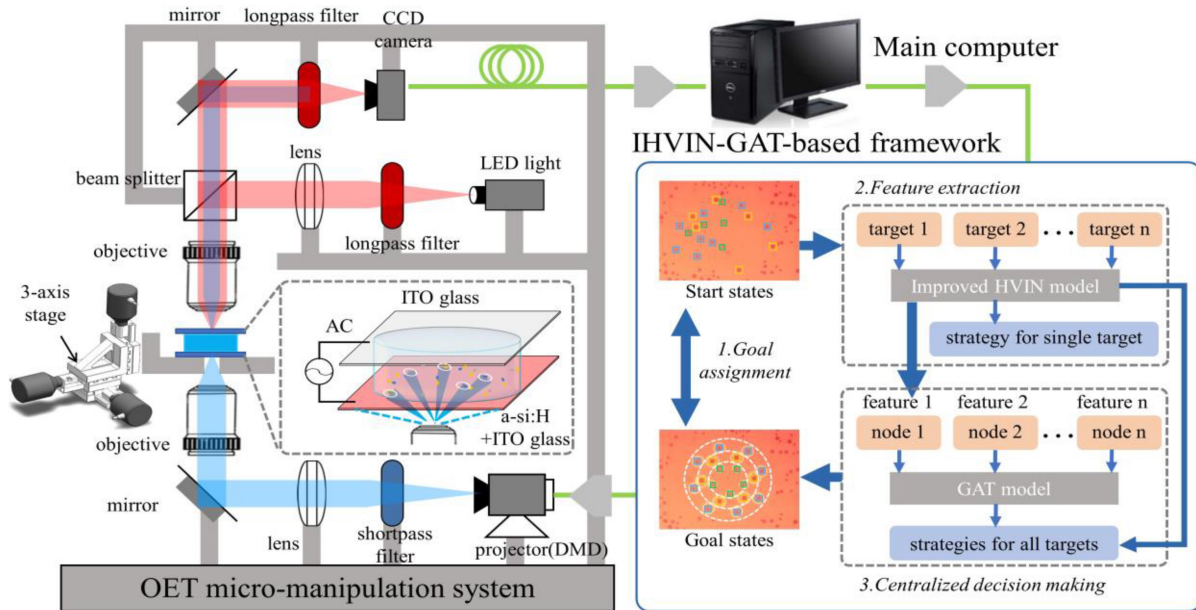


Fig. 1. Schematic of the overall process of IHVIN-GAT-based decision-making framework for parallel manipulation of multiple microtargets with independent control in OET micromanipulation system.

benchmark algorithms in terms of single-target path planning.

- 3) The IHVIN-GAT network performs considerable in compatibility for microtarget's number, keeps the decision-making method from frequent retraining for manipulation tasks where the microtarget's number differs from that in the training set.

This article is organized as follows. Section II presents the background of the OET system and the problem formulation. A well-developed decision-making framework based on the aforementioned IHVIN-GAT model is introduced in Section III. The simulation and experimental evaluations are provided in Section IV. Section V concludes this study.

II. BACKGROUND AND PROBLEM FORMULATION

Multiagent path planning algorithms that enable each robot to reach the goal points accurately and securely have remained in a challenging state even in macro application scenarios (such as autonomous vehicles and multiple UAVs) [40], [41]. In addition, the complexity of unstructured liquid environments at microscale and properties of the OET mechanism bring extra constraints. Therefore, analysis of microobject's locomotion in OET systems and interaction between multitar-

this study, we adopt virtual electrodes in the shape of a ring, so microparticles trapped in the ring's center can be pushed away toward any directions by repulsive force. An LED light provides a source of illumination to enhance the visual images observed via charge-coupled device camera. According to [42], a-si:H layers have a weaker absorption coefficient for light beams with long wavelengths than short wavelengths, resulting in less dielectrophoretic (DEP) force. Therefore, a long-pass filter is utilized after the LED light and optical patterns from projector are limited to shorter wavelengths via a short-pass filter. A three-axis stage controls the movement of OET chip and expand the working space.

B. Constraints for Decision Making

To some extent, the decision-making tasks can be converted into a process of seeking feasible or even optimal solutions under constraint configurations. However, the safe radius as constraints in general methods is time-varying, especially in a liquid environment with heterogeneous obstacles. Since the boundary condition for escape phenomenon of a microtarget shifts according to the adjacent virtual electrodes and microparticles with differentiated electrical characteristics instead of remaining constant. Modifying the value of constraints in real time based on the current environment status is an extremely intricate and costly task. Consequently, we conduct experimental explorations and simulation analysis to study the escape mechanism, aiming at developing a series of fixed constraints to address time-varying challenging.

The team starts with a series of collision tests to explore the minimum distance between two controlled microparticles. As shown in Fig. 2(a), the experimental details are as follows. Transporting two polystyrene microbeads trapped by virtual electrodes toward each other with the smallest possible velocity (nearly equal to 0), until the green microbead escape from

A. System Setup

The structure of OET manipulation system is shown in Fig. 1. Programmable optical patterns are generated in a digital projector and focus on the photoconductive layer (a-si:H) in the OET chip through a condenser lens and an objective. The a-si:H layer coated on the indium tin oxides substrate is illuminated to change the conductivity of the local area, so that virtual electrodes are generated and microtargets within the layer are actuated by dielectrophoretic force. In

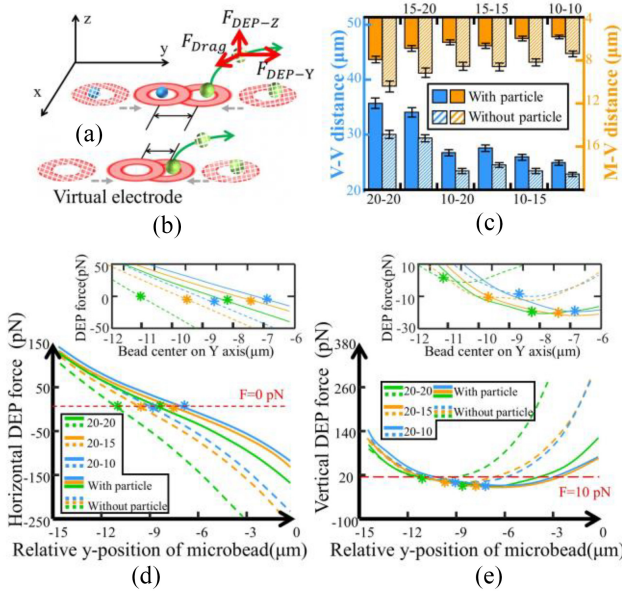


Fig. 2. Analysis of locomotion constraints in OET system. (a) and (b) Schematic illustrating the experiments setup to explore mutual escape boundary conditions under mutual interference. (c) Experiment results, including V-V distance and M-V distance under different conditions. Simulation results of DEP force in horizontal (d) and vertical (e) directions under critical states of escape, respectively.

virtual electrode. In addition, collision tests between a single virtual electrode and a virtual electrode with trapped particles are also conducted, as shown in Fig. 2(b). At the boundary moment of escape, the distance between the two virtual electrodes' centers (V-V distance), and the distance between the center of green microbead with corresponding virtual electrode's center (M-V distance) are expressed statistically in Fig. 2(c). The label on the x -axis in Fig. 2(c), “15-20” indicates that the diameter of the left bead in Fig. 2(a) (same virtual electrode in Fig. 2(b) but without particle) is $15 \mu\text{m}$ and the diameter of right bead in Fig. 2(a) and (b) is $20 \mu\text{m}$. The legends in Fig. 2(c), “with particle” and ‘Without particle’ indicate the corresponding data are from collision tests in Fig. 2(a) or (b), respectively. The data in Fig. 2(c) show that the safe radius of a trapped microparticle is not constant, but is related to the adjacent microparticle and virtual electrode. Moreover, the smaller V-V distance and larger M-V distance from ‘Without particle’ data than from with particle data indicates that, microparticles repel each other.

To further analyze the escape mechanism, we take the $20 \mu\text{m}$ polystyrene microbead as the focused target, and perform six sets of simulation in COMSOL multiphysics. The simulation setup replicates the state at the boundary moment of escape. More specifically, the distance between two virtual electrodes in simulation setup is equal to the V-V distance in Fig. 2(c). The horizontal DEP force and vertical DEP force on the microbead along the y -axis are recorded in Fig. 2(d) and (e), respectively. The x -axis coordinates indicate the relative position of the microbead's center with respect to the center of virtual electrode on the y -axis. Position of microbead at each boundary moment of escape is marked with “**” on two subfigures based on the experimental data M-V distance. From

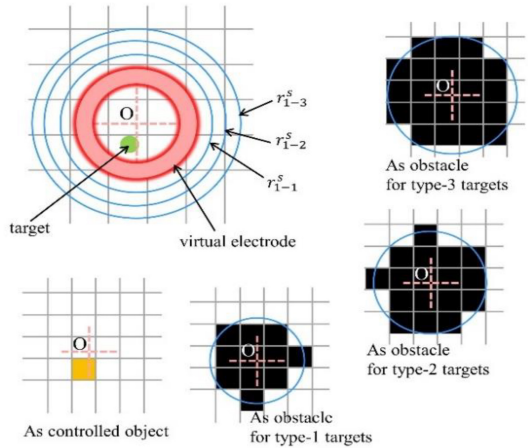


Fig. 3. Differentiated occupied area in grid world for a microparticle when it exists as a controlled object or an obstacle for diverse types of microtargets.

the simulation results, we can see that the horizontal DEP forces of all microbeads at the boundary moment of escape are close to 0 pN . The reason is that microsphere moves at a very small velocity in experiment, thus the velocity can be assumed to be 0. Based on the Stokes's law, the horizontal DEP force on the microbead is almost equal to 0

$$F_{H_DEP} = F_{Drag} = 6\pi\eta rv \quad (1)$$

where η represents the viscosity of the solution, r represents the radius of the microparticle, and v refers to the velocity of microbead. Inertial forces are negligible due to scale effects.

In addition, the vertical DEP forces of all microbeads at the boundary moment of escape are smaller than 10 pN . The vertical DEP force generates velocity on z -axis, which renders the microtarget uncontrollable. Thus, the mechanism of microparticle escape has been basically revealed as follows.

- 1) *Velocity Determines Position:* The position of microparticle in virtual electrode is not arbitrary, and velocity of microtargets is directly proportional to the position's horizontal DEP force, according to (1).
- 2) *Vertical DEP Force Determines Whether Escape Occurs:* Whether the microparticle will escape is mainly determined by the vertical DEP force at current position. The microparticle escapes when the vertical DEP force is greater than a certain threshold (approximately 10 pN)

In this study, the escape mechanism of microparticle is proposed as a universal theoretical basis to numerically calculate the interaction-safe distance r_{i-j}^s between two microtargets. All discrete interaction-safe distances in a heterogeneous system are collected as spatial fixed constraints to replace the time-varying safe radius of single microtarget.

C. Problem Statement

We simplify the workspace for manipulation of heterogeneous multitargets into a 2-D grid world, which is suitable for computing on GPUs. Mathematical definitions of some basic concepts are provided as follows.

- 1) *State of Target Microparticles:* Let $V = \{v_{1-1}, v_{1-2}, \dots, v_{n-m}\}$ be the set of all target microparticles, where v_{i-j} is to the j th microparticle

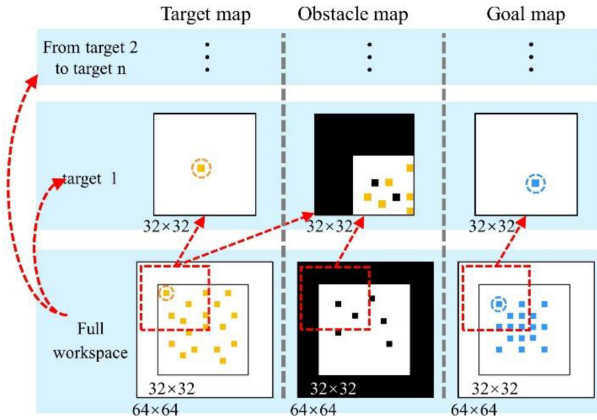


Fig. 4. Input data for IHVIN-GAT model.

belonging to the i -th type. The current positions of targets are $X_t = \{x_{1-1}, x_{1-2}, \dots, x_{n-m}\}$.

- 2) *State of Goal Positions*: Let $G = \{g_{1-1}, g_{1-2}, \dots, g_{n-m}\}$ be the set of state of goal positions, where g_{i-j} is not the goal position for microparticle v_{i-j} , but rather the j -th goal position for microparticles of i -th type.
- 3) *Interaction-Safe Distance*: In the set $R^S = \{r_{1-1}^S, r_{1-2}^S, \dots, r_{p-q}^S\}$, r_{i-j}^S is the interaction-safe distance between a microparticle of i -th type and a microparticle of j -th type, respectively.
- 4) *State of Actions*: In the set $A_t = \{a_{1-1}^t, a_{1-2}^t, \dots, a_{n-m}^t\}$, a_{i-j} is the action for v_{i-j} , and involves up, down, left, right, up-left, up-right, down-left, down-right, and stop. In each control period, a target executes the action only once.
- 5) *State of Obstacles*: Let $O = \{O_{1-1}, O_{1-2}, \dots, O_{n-m}\}$ be the set of obstacle states for all target microparticles. $O_{p-q} = \{o_1, o_2, \dots, o_k, o_{1-1}^t, o_{1-2}^t, \dots, o_{n-m}^t\}$ is the set for a certain microtarget v_{p-q} , where o_i is the randomly distributed microobject in liquid environment and o_{i-j}^t refers to other controlled microtarget. $\forall i, j (i \neq p) \parallel (j \neq q)$.

To enable the decision-making method fully learning the heterogeneous information of the system, a microtarget occupies different areas in grid world when it exists as an obstacle for diverse categories microtargets. As shown in Fig. 3, the occupied area is mainly determined by the locomotion constraints between two microtargets (interaction-safe distance, r_{i-j}^S). To be consistent with locomotion constraints, the center of the virtual electrode is set as the center of the occupied area, since the interaction-safe distance is calculated based on the V-V distance as described in Section II-B.

III. DYNAMIC CONTROL FRAMEWORK

In this study, the task of manipulating multiple microtargets to goal positions can be divided into three parts: 1) optimal assignment of goal positions for microtargets of the same type; 2) high-ordered feature extraction for individual microtargets via an IHVIN model; and 3) decentralized decision-making for all microtargets through selective aggregation of features from neighboring microtargets in graph attention networks.

A. Input for IHVIN-GAT Model

The input map of the IHVIN, including the state of microtargets, goal positions, and environment information, as shown in Fig. 4. When a microtarget is considered, other targets are represented as obstacles in the occupancy map. The target-centered mode is adopted for input maps since it can unify the process of extracting patches around microtargets in IHVIN, regardless of the position of microparticles in workspace. Thus, a virtual workspace with twice the original side length is expanded across the three input maps. The expanded area is padded with 0 in original target map and goal map, and padded with 1 in original occupancy map as obstacles. Then, three patches centered on the state of considered microparticle are, respectively, extracted from the expanded maps, and the patch size is the same as the original map size. Obviously, the length scale and relative positional relationship among microobjects stay fixed. When the goal state is far enough away from the current state to exceed the bounds of patches, a point on the edge in goal map is marked to indicate the goal's direction. The input map, also called the observation of v_{i-j} is expressed as M_{i-j} .

B. Goal Assignment

Assigning goal position to the most appropriate microtarget rather than arbitrarily assignment can enhance the efficiency of manipulation. In this study, a goal assignment method is proposed and periodically executed to modify the matching scheme between microtargets and goal positions. One goal position of a specific type can only be matched to the same microparticle types. The estimated cost between a microparticle and a specific goal position is denoted as

$$E_{i-j} = D_{i-j} + \sum_{w=1}^{m-1} \gamma_{i-j}^w R_{\text{sys}}(\pi - 1) + \lambda \sum_{k=1}^p \left[\cos^{-1} \left(\frac{L_{i-j}^k}{R_{\text{sys}}} \right) - \sqrt{R_{\text{sys}}^2 - L_{i-j}^k} \right] \quad (2)$$

where E_{i-j} refers to the estimated cost between the i -th microparticle and the j -th goal position; D_{i-j} is the Manhattan distance between the current position of the i -th microparticle to the j -th goal position; the second and third terms are the extra cost of avoiding collision with other microtargets or obstacles, respectively; γ_{i-j}^w and λ are the discount factor; R_{sys} is the estimated radius of detour path; and L_{i-j}^k is the off-set distance of the k -th obstacle relative to the straight line from the current position of the i -th microparticle to the j -th goal position.

In addition to Manhattan distance, the extra detour distance for collision avoidance with obstacles are also taken into account in the estimated cost. To minimized the total transporting cost, the reward function is optimized as

$$\max R = - \sum_{i=1}^m E_{i-p(i)} + C, p(i) \in \{1, 2, \dots, m\} \\ \text{s.t. } \forall i, j \in \{1, 2, \dots, m\}, i \neq j : p(i) \neq p(j). \quad (3)$$

An optimization approach based on the Kuhn–Munkres algorithm is applied to find the optimal matching scheme

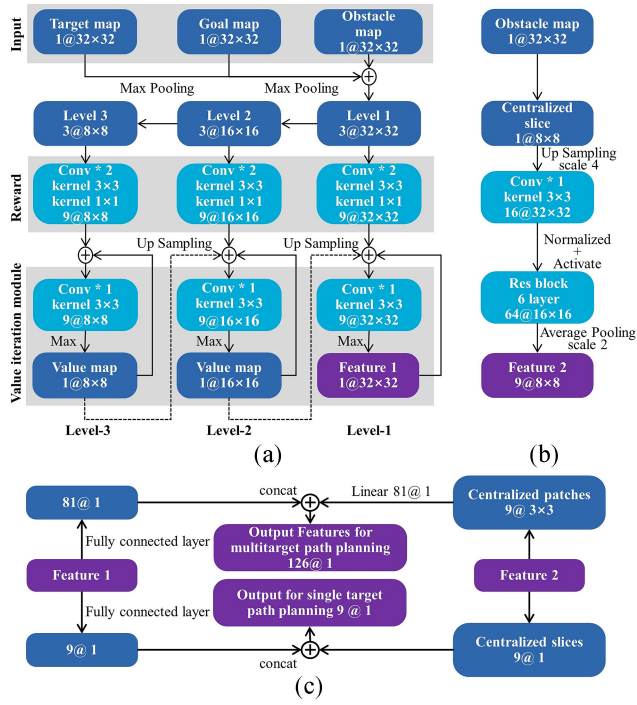


Fig. 5. IHVIN model for feature extraction and single-target path planning. Structure of (a) HVIN and (b) ResNet blocks. (c) Output features for multi-targets path planning and output for single-target path planning.

for the goal assignment. An adjacency matrix is established, where the element in the i th row and j th column of the matrix represents the estimated costs for the i th microtargets to the j th final position. The adjacency matrix is calculated through the following five steps: 1) row reduction; 2) column reduction; 3) test for an optimal assignment; 4) shift zeros (if requires); and 5) completing final assignment, which are introduced detailly in [43]. Steps 3 and 4 are iteratively repeated until the optimal matching scheme is found. The Kuhn–Munkres algorithm satisfy permutation equivariance, that is, this method always gives the same matching scheme regardless index changes.

C. Feature Extraction via IHVIN Model

Inspired by the idea of iteratively calculating long-term reward in value iteration algorithm, value iteration networks (VINs) demonstrate stronger capability to conventional neural network architectures in path planning. By rewriting the Bellman equations as convolution operation, the backpropagation process can be utilized in the VIN module to learn the long-term goal-directed behaviors of planning. The rewritten Bellman equations can be described as

$$V_{i-j} = \max_a Q(a|x_{i-j}) \quad (4)$$

$$Q(a|x_{i'-j'}) = \sum_{l,i,j} W_{l,i,j}^a [R(x_{i-j}|x_{i'-j'}) + V_{i'-j'}] \quad (5)$$

where $W_{l,i,j}^a$ refers to an element in convolution kernel W^a ; $R(x_{i-j}|x_{i'-j'})$, $Q(x_{i-j}|x_{i'-j'})$, and V_{i-j} are the features corresponding to the conception of reward, Q function, and value function in value iteration algorithm.

TABLE I
ARCHITECTURE OF RESNET BLOCKS

Layer name	Output size	(kernel size, feature, stride)
Layer_1	16×16	$\begin{cases} 1 \times 1, 16, 1 \\ 3 \times 3, 16, 2 \\ 1 \times 1, 64, 1 \end{cases} \times 1$
From Layer_2 to Layer_6	16×16	$\begin{cases} 1 \times 1, 16, 1 \\ 3 \times 3, 16, 1 \\ 1 \times 1, 64, 1 \end{cases} \times 5$

Furthermore, hierarchical VINs (HVINs) are proposed to increase the convergency velocity via coarse-to-fine planning. The input maps are downsampled to low-resolution maps and then fed into value iteration module to generate state-value estimates. The state-value estimates are then upsampled as the initialization of high-resolution value map. HVIN can still be improved in feature extraction.

In this study, we originally develop the improved IHVIN model with a parallel architecture to learn the long-term goal-directed features and local environment features, respectively. The abstract features of the former are extracted through a three-layer HVIN network, as shown in Fig. 5(a). Input maps containing information on microtarget position, goal position, and environment are generated. Levels-2 and 3 input maps with halved resolution are obtained by a max pooling operation on Levels-1 and 2 input maps. Subsequently, reward maps are processed from three levels of input maps after two convolution operations with kernels of size 3×3 and 1×1 . Multiple reward features are required for each unit to represent the abstract information of diverse actions in this state. The features of value estimates with coarse-to-fine resolutions are generated through the value iteration module (after multiple iterations) in three levels. Three modules are organized together in a serial architecture, and the value estimate features in low-level are unsampled as the initialization input for high-level modules. The long-term goal-directed features (*Feature 1*) are generated through *Level-1* value iteration module.

As shown in Fig. 5(b), we introduce a conventional neural network with ResNet blocks to learn local environment information, particularly neighbor obstacles. ResNet block is a well-validated backbone for local feature extraction, of which the architecture is depicted in Table I. A centered patch of size 8×8 is extracted from the obstacle map, then is upsampled (scale 4) and convolved (kernels size 3×3). After process of six-layer ResNet blocks and the average pooling operation, local environment features are extracted and named as *Feature 2*.

The abstract information obtained by the ResNet blocks from local environment information and the HVIN must be integrated to obtain the high-order features for decentralized decision-making. As shown in Fig. 5(c), patches of size 3×3 are extracted from the *Feature 1* and linearized. We also obtain the same dimension data from *Feature 2* through a fully connected layer. Overall features of a single node are obtained by stacking these two data and feeding them into a fully connected layer. The IHVIN model can also generate

real-time locomotion strategies for a single microtarget path planning. Similar to the feature extraction process, but with the distinction that single-target decision making requires only nine features of the centered unit rather than the patches of size 3×3 . The corresponding stacked data from ResNet block are also modified to the same dimension. The optimal locomotion action in one-step for a single microtarget is predicted through the softmax function and argmax function.

D. Decentralized Decision-Making via GAT

Only oversimplifying other microtargets to stationary obstacle states is inadequate for multitarget path planning, the conflict risk between future actions of microtargets still exists. Therefore, a decentralized path planner capable of integrating environmental information, and the tendencies of potential actions is in demand to formulate strategies for all microtargets. Graph neural networks [44] are increasingly applied to multirobot domains because the features of neighboring nodes can be aggregated without severely restricting the number of nodes and edges. We convert the structure of multitarget decision making into a graph as $G_t = (V, \Gamma_t, S_t)$, where $\Gamma_t \subseteq V \times V$ is the set of edges and $S_t(v_{i-j}, v_{p-q})$ refers to the weight of the edge connecting two nodes v_{i-j} and v_{p-q} . The states of neighboring nodes and their potential action tendencies do not have uniform degrees of influence on microtarget decision making. The attention mechanisms of graph attention networks (GAT) [45] are introduced in this study to provides a feasible scheme with selective focus on neighbors' features. The operation of one layer in the GAT can be formulated as

$$F_t^{L+1} = \sigma \left[\sum_{k=0}^{K-1} (\alpha \odot S_t)^k F_t^L W_k \right] \quad (6)$$

where $\sigma(\cdot)$ is an activation function of point-wise nonlinearity; F_t^L refers to the output features of the L -th layer in the form of a matrix, where $F_t^0 = [f_{1-1}', \dots, f_{m-n}']$ is the set of original features extracted from the IHVIN model; W_k of size $F \times G$ refers to the filter that performs graph convolution on aggregated features, where F and G are the dimensions of input and output features; and $(\alpha \odot S_t)^k F_t^L = (\alpha \odot S_t) \times [(\alpha \odot S_t)^{k-1} F_t^L]$ is computed by k -times feature aggregations with 1-hop neighbors. α is the attention matrix and has the same size as S_t . Normalized attention coefficients are computed as follows:

$$\alpha(v_{i-j}, v_{p-q}) = \frac{\exp(e(v_{i-j}, v_{p-q}))}{\sum_{k \in N_i} \exp(e(v_{i-j}, k))}, \quad v_{p-q} \in N_i \quad (7)$$

where N_i is the set of all neighboring nodes of microtarget v_{i-j} , and $e(v_{i-j}, v_{p-q})$ is calculated by $(R^{2G} \times R^{2G} \rightarrow R)$

$$e(v_{i-j}, v_{p-q}) = H(f_{i-j}' W_k \| f_{p-q}' W_k) \quad (8)$$

where H is a shared vector with dimension of $2G \times 1$.

The attention coefficient for node 1-1 is shown in Fig. 6(a). The edge labeled “with connection” connects 1-hop neighbor nodes. Label “receive features” indicates that despite there are no edges connecting node 1-1 and the 2-hop ($K = 2$) or 3-hop

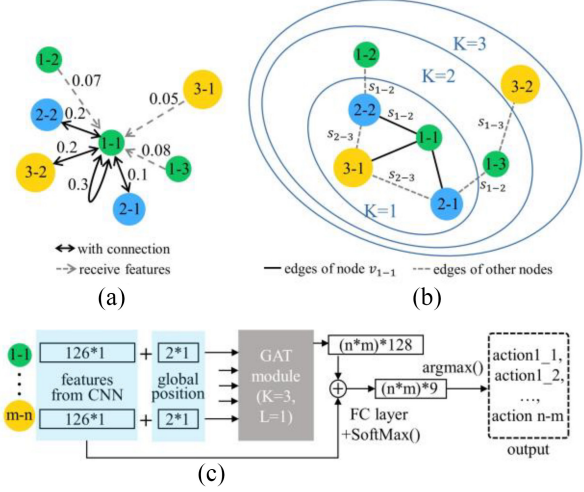


Fig. 6. GAT model for decentralized decision-making. (a) Attention coefficient for node 1-1. (b) Schematic of connection edges between microtargets and the corresponding weights. (c) Network structure for decentralized decision-making.

($K = 3$) neighbor nodes, communication could occur within three-times feature aggregations in GAT.

As the discrete interaction-safe distance is essentially an inductive description of the relationship between two microtargets. In other words, it can be converted into the relationship between two nodes in the graph domain. Therefore, we enhance the attention mechanisms to present the system heterogeneity, by differentiating the conditions and weights for constructing edges connecting different types of controlled microtargets in the isomorphic graph, as follows:

$$S_t(v_{i-j}, v_{p-q}) = \begin{cases} 0, & \text{if } \|x_{i-j} - s_{p-q}\| > \beta r_{i-p}^S \\ s_{i-p}, & \text{if } \|x_{i-j} - s_{p-q}\| < \beta r_{i-p}^S \end{cases} \quad (9)$$

where s_{i-p} is a learnable parameter, refers to the weight of the edges connecting two microparticles belonging to i -th type and p -th type. $\max_{i,p} s_{i-p} = 1$. β is a constant and $\beta > 1$.

Unlike heterogeneous graphs with intricate internal structures and embedding challenges, this method needs to train only an extra C_n^2 parameters (n is the number of types of microparticles) instead of several matrices. The schematic of connection edges between microtargets and the corresponding weights S_t is shown in Fig. 6(b). The Manhattan distance between v_{1-1} and v_{1-3} exceeds the maximum communication radius βr_{1-1}^S , so the corresponding weight $S_t(v_{1-1}, v_{1-3})$ is equal to 0. In other words, no edge exists between two nodes. In contrast, since $\|x_{1-1} - x_{2-1}\| \leq \beta r_{1-2}^S$, the edge connecting v_{1-1} and v_{2-1} exists, and the corresponding weight is s_{1-2} .

As shown in Fig. 6(c), the global position of microparticles is stacked with features extracted via IHVIN, and participates in the calculation of attention coefficients, since the relative position between two microparticles is a critical factor affecting the degree of their mutual interference. In other words, the relative distance between microspheres modulates the weights of feature aggregation in forms of features. The features are convolved to a matrix of size $(m \times n) \times 9$ via a fully connected layer and normalized by softmax. The predicted actions for

Algorithm 1: Decentralized Decision-Making Method

```

Input: target microparticles' state  $X_0$ , goal positions' state  $G$ , obstacles' state  $O$ , and trained IHVIN-GAT model.
Initialize step  $t = 0$ , calculate the locomotion constraints  $R^S$ .
while  $V \neq \emptyset$  do
    Update obstacles' state  $O$  and microtargets state  $X_t$ .
    //Goal assignment every  $T_G$  times.
    if  $t \bmod T_G = 0$  then
        for  $i = 1$  to  $n$  do
            Do goal assignment for microtargets of type  $i$ .
            Modify the internal order of  $\{g_{i-1}, \dots, g_{i-m}\}$ .
        end for
    end if
    for  $v_{i-j}$  in  $V$  do
        Extract features  $f_i - j^t$  of  $v_{i-j}$  via IHVIN.
        Store  $f_i - j^t$  in  $F^t$ .
    end for
    Generate graph  $G_t = (V, \Gamma_t, S_t)$  at step  $t$ .
    Calculate actions  $A_t = \{a_{1-1}^t, a_{1-2}^t, \dots, a_{n-m}^t\}$  via GAT.
    //Check and modify the actions before execution.
    while  $(X'_{t+1}|X_t, A_t)$  does not satisfy the constraints:
        | Update actions  $A_t$  via expert algorithm
    end while
    Execute actions  $A_t$ .
    //Check if the microtarget has reached the goal position.
    for  $v_{i-j}$  in  $V$  do
        if  $v_{i-j} = g_{i-j}$  then
            | Remove  $v_{i-j}, g_{i-j}$  from  $V$  and  $G$ .
        end if
    end for
     $t = t + 1$ 
end while

```

all microtargets are generated by an action policy on the probability distribution over the candidate actions.

E. Workflow of the Proposed Control Framework

The decision-making procedure for parallel manipulation of multiple microtargets is summarized in Algorithm 1. The process of goal assignment executes once every T_G actions to dynamically modify the matching scheme of microtargets and goal positions, where T_G is an integer, and is determined with tradeoff between time consumption and trajectory efficiency. Due to the task intricacy and the inherent limitation of the learning-based model, 100% task success cannot be guaranteed. Meanwhile, the task failure risk will increase exponentially when more microtargets are manipulated simultaneously. In this regard, we verify whether the predicted actions conflict with locomotion constraints before action execution. If conflict occurs, alternative actions will be generated by the expert algorithm (introduced in Section IV) to guarantee the task complement. If a microtarget have reached goal position, it is considered a fixed obstacle and does not participate in decision making no longer.

To manipulate microtargets automatically in OETs systems, we grayscale and denoise the microscopic image, then utilize the Hough circle detection algorithm for real-time positioning of microtargets. To accurately follow the predicted actions, the proxy-based sliding mode control (PSMC) method is employed for trajectory tracking by regulating the velocity

of virtual electrodes. These two methods are introduced comprehensively in our previous work [46].

IV. SIMULATION COMPARISONS AND EXPERIMENTAL STUDIES**A. Dataset Creation and Training**

In this study, we introduce the idea of imitation learning to train our IHVIN-GAT model with the data yielded by an expert algorithm. The expert algorithm we adopt for imitation learning is the conflict-based search (CBS) method. The CBS method is an optimal solver for broad MAPF problem, and the generated strategies share a unified internal logic. To learn from the real-world manipulation tasks as closely as possible in the training data, we collected 1500 decision-making cases from 50 experiments with heterogeneous microtargets (composed of 10 μm , 15 μm , and 20 μm diameter polystyrene microbeads, with a total concentration of $600 \pm 300 \mu\text{L}^{-1}$). Among these cases, 1000 are utilized for training, 150 for validation, and 350 for testing. The reference actions vectors are computed by the expert algorithm, a vector comprises actions for all microtargets at step t . A training data unit is composed of an action vector $U_i^t = [u_{1-1}^t, u_{1-2}^t, \dots, u_{n-m}^t]$ coupled with the corresponding observation maps $M_i^t = \{m_{1-1}^t, m_{1-2}^t, \dots, m_{n-m}^t\}$. The set of training data is a collection $\Phi = \{(U_i^t, M_i^t)\}$, $i = 1, 2, \dots, 1000$, $t = 1, 2, \dots, t^{\max}$. One-step strategies based on an “instant” situation, rather than full paths are learned for the IHVIN-GAT model during training. The objective of training is to reduce the loss function between expert actions and predicted actions by adjusting the learnable parameters P :

The objective of training is to reduce the loss function by adjusting the learnable parameters P

$$\hat{P} = \arg \max_P \sum_{(U_i^t, M_i^t) \in \Phi} \text{Loss}(U_i^t, \text{Model}(M_i^t)). \quad (10)$$

Furthermore, extra data are generated to evaluate performance of the IHVIN model for single-target path planning.

B. Metrics for Evaluation

Three metrics to evaluate the performance of the proposed decentralized decision-making model is proposed.

- 1) *Accuracy Rate*: $AR = \frac{\sum_{i,t} \text{sum}(|\text{sgn}(U_i^t) - \text{Model}(M_i^t)|)}{\sum_{i,t} 1}$, is the ratio of actions predicted by networks to that are consistent with expert' strategies on the validation set.
- 2) *Success Rate*: $SR = n_{\text{success}}/n_{\text{test}}$, refers to the proportion of successful cases to the total number of tested cases n .
- 3) *Path Increase*: PI represents the ratio of extra path length predicted by networks to trajectory generated by the expert algorithm.

C. Evaluation in Simulator

We successively verify the performance of the IHVIN model applied to single-target path planning [in Fig. 7(a)–(c)] and the

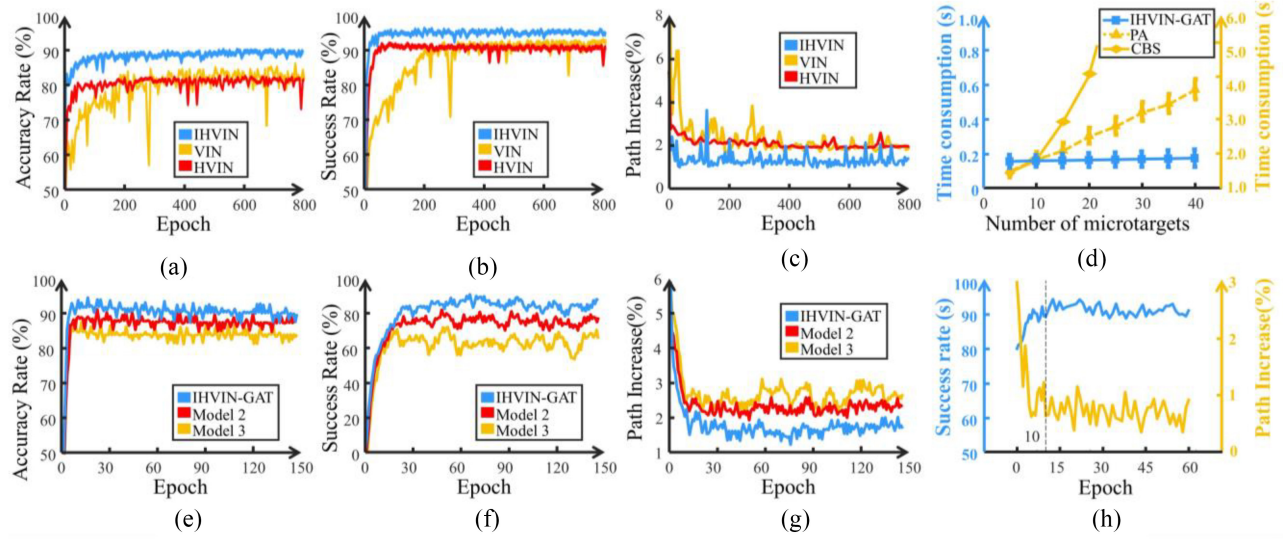


Fig. 7. Simulation results of decision making. The IHVIN outperforms the benchmark algorithms in terms of accuracy rate (a), success rate (b), and path increase (c). (d) Computation time of diverse model for multitarget decision making versus the number of microtargets. IHVIN-GAT model outperforms the benchmark algorithms in terms of (e) accuracy rate, (f) success rate, and (g) path increase. Model 2 in (e)–(g) is the IHVIN-GAT model without enhanced attention mechanism. Model 3 in (e)–(g) is the HVIN-GAT model without enhanced attention mechanism. (h) Convergence performance of the trained model for task with diverse microtarget's number.

IHVIN-GAT-based model for multitarget decision making [in Fig. 7(d)–(h)]. Fig. 7(a) indicates that HVIN and the IHVIN model are less prone to becoming stuck in local minima, and have faster convergence velocity than VIN at equivalent iteration counts, owing to the utilization of coarse-to-fine long-term feature extraction. VIN and HVIN manifest undesirable performance in three metrics, frequently encounters task failures like physical collisions and escape accidents in experiments, which results from inadequate extraction of local information around microparticles, e.g., spatial distribution and intensity of electrokinetic interference. In contrast, IHVIN with a parallel architecture learns both local environment via ResNet blocks and long-term goal-directed information via HVIN, since HVIN and ResNet blocks proficient in learning the iterative features and extracting local features, respectively. The IHVIN model appropriately balances the influence of two features on decision making via learnable parameters, enabling accommodating both high-precision obstacle avoidance and approaching the goal position. Consequently, the IHVIN model outperforms VIN and HVIN in terms of both three metrics, demonstrating stronger learning capability [Accuracy Rate in Fig. 7(a)] in terms of path planning, more robust [Success Rate in Fig. 7(b)] and efficient [Path Increase in Fig. 7(c)] for micromanipulation tasks in OETs systems.

Parallel computing of the IHVIN-GAT model on the GPUs facilitates computation efficiency and enhances real-time performance. Fig. 7(d) illustrates the correlation relationship between diverse method's computation time for decision making with the microtarget's number. Competing methods, the CBS method and priority assignment (PA) method are included for comparison. The POMDPs algorithm serves as a low-level search scheme for both two methods. The time cost of the CBS method increases exponentially as the number of microtargets increases, whereas the PA method's time cost is linear to the

TABLE II
COMPATIBILITY OF THE IHVIN-GAT MODEL

Microtarget's number	AR (%)	SR (%)	PI (%)
13	97.2 ^{+2.1} _{-3.7}	94.7 ^{+3.9} _{-5.2}	1.08 ^{+0.31} _{-0.45}
15	95.9 ^{+3.5} _{-2.8}	93.5 ^{+4.0} _{-4.8}	1.23 ^{+0.51} _{-0.54}
17	94.2 ^{+3.9} _{-3.5}	92.9 ^{+3.9} _{-5.2}	1.47 ^{+0.42} _{-0.48}
19	92.7 ^{+2.7} _{-4.6}	89.6 ^{+3.8} _{-4.6}	1.73 ^{+0.46} _{-0.47}
21	90.1 ^{+3.7} _{-2.9}	87.8 ^{+4.1} _{-4.4}	2.01 ^{+0.53} _{-0.36}
23	87.1 ^{+4.0} _{-3.4}	83.1 ^{+4.3} _{-5.6}	2.43 ^{+0.44} _{-0.52}
25	84.3 ^{+4.2} _{-4.2}	80.9 ^{+5.4} _{-4.9}	2.96 ^{+0.56} _{-0.51}

number of microtargets. The average computation time of the IHVIN-GAT model could maintain within 0.2 s regardless of the microtarget's number, demonstrating the superiority in computational efficiency.

The performance of the IHVIN-GAT model for multitarget decision making is demonstrated through comparisons with two benchmark algorithms: 1) the IHVIN-GAT [Model 2 in Fig. 7(e)–(g)] and 2) the HVIN-GAT [Model 3 in Fig. 7(e)–(g)] both without the edge's weight associated with discrete constraints). IHVIN-GAT model and Model 2 both utilize IHVIN method with parallel architecture to extract features, Model 3 utilize the HVIN model to extract features. Neither Models 2 and 3 adopt the enhanced attention mechanism as (9). As shown in Fig. 7(e)–(g), the IHVIN-GAT model and Model 2 outperform Model 3 in both three metrics, demonstrates the stronger capability of IHVIN in extracting and representing features relevant to path planning. Despite Model 2 performs considerable for manipulating one-type microtargets, it is prone to unnecessary detours or escape accidents in tasks with heterogeneous microtargets, since it

ignores the dependence of electrokinetic interference with microtarget's category. In contrast, three metrics of IHVIN-GAT network significantly outperform Model 2 in tasks with heterogeneous microtargets, since the system heterogeneity is exhaustively represented by the enhanced attention mechanism. The edge's configuration associated with discrete constraints facilitates microtargets to selectively allocate attention toward microtargets in accordance with their categories during feature aggregation.

In this study, we focus on the compatibility performance of the trained model in manipulation tasks with variable number. Training the model parameters individually for each manipulation task with diverse number configuration is extremely costly. The proposed IHVIN-GAT Model is trained with a data set where microtargets collections are composed of 18 polystyrene microbeads with diameters of $10\ \mu\text{m}$, $15\ \mu\text{m}$, and $20\ \mu\text{m}$, and the number of each type is 6. Micromotors with diverse sizes manifests differential electrical characteristic, thus presenting the system heterogeneity in experiment. The compatibility of the trained model applied for path planning tasks with diverse numbers of microtargets is illustrated in Table II. The trained IHVIN-GAT Model maintains *success rate* higher than 80% and *Path Increase* lower than 3% as microtarget's number increases to 25, demonstrating satisfactory adaptations to different tasks. Based on the trained parameters of IHVIN-GAT model, we further train the model for tasks with 25 microtargets. As shown in Fig. 7(h), the model converges to optimal performance within 10 epochs, indicating that the trained model can shorten training process of manipulation tasks with different microtarget's number, inspired by transfer learning.

In this study, many parameters in the IHVIN-GAT model are learnable and could be optimized during training, which facilitates the algorithm generalization (e.g., s_{i-j} , the weight of the edge, is trained to represent the system heterogeneity). Learning rate and batch size are two hyperparameters associated with the training procedure. When the learning rate decreases, training stability improves but convergence velocity slows down. Increasing batch size facilitates avoiding local optimal solutions, but is limited by the computer configuration. The learning rate and batch size are set as 0.001 and 64, respectively. The ratio of maximum distance between the connected microtargets to interaction-safe distance (β , introduced in (9)) regulates the spatial range of feature aggregation. Too small β results in increased task failure, while too large β necessitates more training cost to learn key information from redundancy aggregated features. β is set as 4, balancing the success rate and training time efficiently.

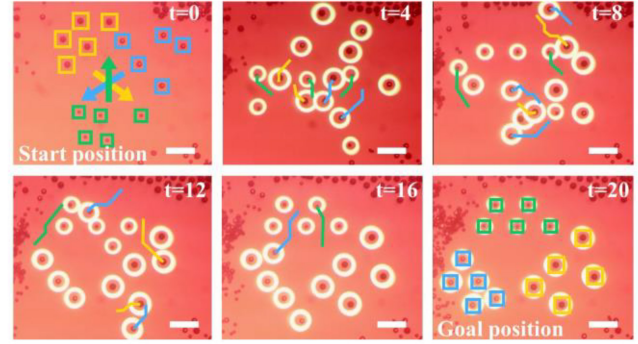
The procedure of goal assignment is executed periodically once every T_G actions to dynamically modify the matching relationship of microtargets and goal positions. As shown in Table III, executing the proposed goal assignment method only once before decision making significantly reduces the micro-manipulation complexity compared to random assignment. Increasing the frequency of goal assignment can further reduce the required paths, especially more effectively for micromanipulation tasks with more microtargets. The reason is that original matching relationship cannot remain optimal during

TABLE III
NORMALIZED PATH LENGTH UNDER DIFFERENT EXECUTION FREQUENCIES OF GOAL ASSIGNMENT

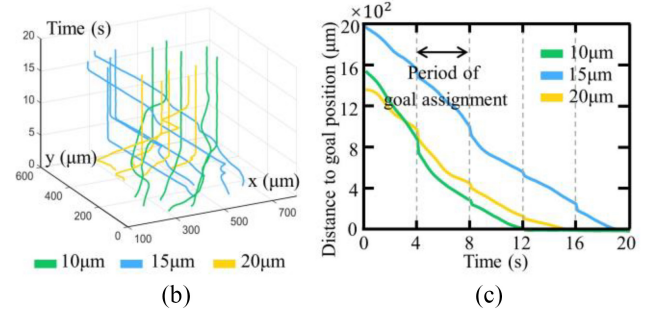
Microtarget's number	$T_G = 1$	$T_G = 4$	$T_G = 7$	Once	Zero
8	64.72%	65.49%	66.35%	67.13%	1
10	63.42%	64.39%	65.45%	66.76%	1
12	61.70%	62.75%	63.97%	65.33%	1
14	58.49%	59.90%	62.31%	63.62%	1
16	55.72%	58.73%	60.16%	62.82%	1
18	53.13%	56.31%	58.12%	60.98%	1
20	51.21%	53.58%	56.34%	59.24%	1
22	48.74%	51.16%	54.46%	57.76%	1
24	45.82%	49.26%	52.69%	56.13%	1

TABLE IV
COMPUTATIONAL TIME OF GOAL ASSIGNMENT

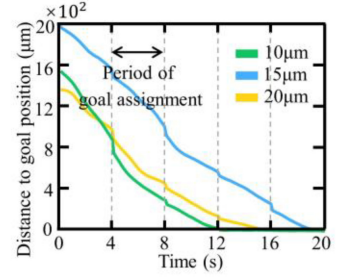
Microtarget's number	8	12	16	20	24
Average Time (ms)	23	76	248	503	1673



(a)



(b)



(c)

Fig. 8. Experimental results to evaluate the quality of the predicted actions. (a) Snapshots of this experiment at six different times. (b) Full trajectories of microtargets. (c) Sum distance from the current position of all one-type microparticles to the goal positions. Scale bars, $100\ \mu\text{m}$.

locomotion of microtargets. However, the computational time of goal assignment proliferate exponentially as the number of microtargets increases, as shown in Table IV. Through the tradeoff of computational time and trajectory efficiency, T_G is set as 4 s/time.

D. Experimental Examples

Experimental examples are carried out to verify the effectiveness of the IHVIN-GAT Model in manipulation tasks with

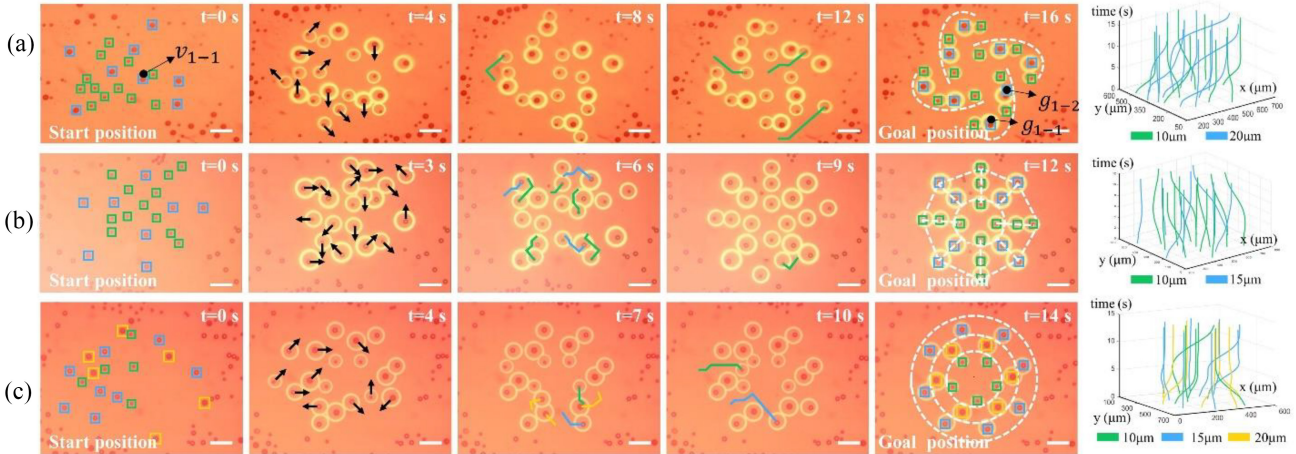


Fig. 9. Experimental results of patterned assembly in horizontal plane of microtargets. (a) Pinwheel-shaped pattern. (b) Radial pattern mimicking the hepatic lobules. (c) Ring pattern mimicking the vascular walls. Scale bars, 100 μm .

heterogenous microtargets. An extreme experiment is designed to evaluate the quality of the predicted actions, as shown in Fig. 8(a) and the attached video (S1). The start positions of three types of polystyrene microbead clusters are distributed in form of triangles. The target positions for each type of microbead are set to the opposite side of the workspace from their start positions. For instance, five polystyrene microbeads with a diameter of 20 μm start from in upper-left corner and are finally transported to the lower-right corner in workspace. Naturally, high frequency rendezvous microparticles occurs in the center of the workspace, and the risk of potential collisions is greatest here. This experimental design is inspired by the international game of checkers. The temporal and spatial dimension complexity in this experimental design intentionally heighten the challenge of multitarget decision making, for verifying the ability of the proposed model in collision-avoidance and escape-avoidance. Partial trajectories and complete trajectories of microtargets are shown in Fig. 8(a) and (b), respectively. The entire transport task is completed within 20 s. Fig. 8(c) illustrates the sum distance from the current position of all one-type microparticles to goal positions versus time. For instance, the total distance of “ith” type is described as ϑ_i^t

$$\vartheta_i^t = \sum_{j=1}^m (\|x_{i-j} - g_{i-j}\|_2). \quad (11)$$

Fig. 8(c) illustrated that the distance from current positions to goal positions decreases all times, while avoiding the escape and collision risks of high spatiotemporal densities in such extreme tasks. The distance suddenly decreases when goal assignment is executed, since the matching scheme is reformulated and optimized based on the current state.

Further experiments are conducted to demonstrate the great application potential of the decision-making method for micropatterning scenarios. As shown in Fig. 9(a), a pinwheel-shaped pattern is formed within 16 s by transporting eight microparticles with a diameter of 20 μm , and 12 microparticles with a diameter of 10 μm . These microparticles are initially randomly distributed throughout the

workspace. Microparticles of two types arranged to alternate on each “blade” of the “pinwheel,” demonstrating that our proposed manipulation method is able to achieve single-object-level accuracy while remaining highly efficient. The microparticle v_{1-1} is eventually transported to the goal position g_{1-1} , even though g_{1-2} is closer to the starting position of v_{1-1} . This is because the goal assignment algorithm aims a global optimal solution for all microtargets. In addition, a radial pattern mimicking the hepatic lobules and a nested ring pattern mimicking the vascular walls are developed as shown in Fig. 9(b) and (c). Experimental details for the patterned assembly can be found from the attached video (S2). This result indicates the compatibility of the aforementioned methods for tasks with different numbers of microtargets, and the feasibility and potential for biological micropatterning tasks.

In experiments, a few failure cases occur when more than three conflict risks simultaneously exist on a single microtarget, predicted actions manifest insufficient attention to conflict risks other than the most critical ones. In this regard, targeted extra training of the data associated with these intricate situations may facilitate improving success rate of the proposed IHVIN-GAT method in multiagent path planning.

V. CONCLUSION

In this study, we propose a dynamic decision-making method for manipulation tasks with heterogeneous microtargets, such as micropatterning. Through simulation and experimental analysis in terms of escape mechanism, discrete interaction-safe distance in OET systems is developed to replace the variable locomotion constraints. The IHVIN-GAT model extracts and balances the long-term goal-directed and local environment features via a parallel architecture, enabling accommodating both high-precision obstacle avoidance and approaching the goal position. High-order features from other microtargets are selectively aggregated and convolved to void collision or mutual interference. By configuring weight of the edge in graph domain based on the discrete locomotion constraints, the attention mechanism is enhanced to represent the system heterogeneity, facilitating microtargets to

selectively allocate attention toward microtargets according to their categories during feature aggregation. The simulation and experimental examples, verify the significant performance of the proposed methods in terms of the quality of the extracted features, predicted actions, time consumption, and compatibility for different numbers of microtargets.

To the best of our knowledge, there are no works for parallel manipulation with heterogeneous microtargets using the MAPF algorithm in real-world scenarios. We believe that IHVIN-GAT-based dynamic decision-making methods combined with an OET system will be an inspiring research direction for biomedical scenarios, including micropatterning. Furthermore, we believe that the aforementioned method will contribute to general path planning research with heterogeneous multirobot systems.

REFERENCES

- [1] Z. Zhang, X. Wang, J. Liu, C. Dai, and Y. Sun, "Robotic micromanipulation: Fundamentals and applications," *Annu. Rev. Control Rob. Auton. Syst.*, vol. 2, pp. 181–203, May 2019.
- [2] S. Bhatia, U. Balis, M. Yarmush, and M. Toner, "Effect of cell-cell interactions in preservation of cellular phenotype: Cocultivation of hepatocytes and nonparenchymal cells," *FASEB J.*, vol. 13, no. 14, pp. 1883–1900, Nov. 1999.
- [3] M. Y. Chiang, Y.-W. Hsu, H.-Y. Hsieh, S.-Y. Chen, and S.-K. Fan, "Constructing 3D heterogeneous hydrogels from electrically manipulated prepolymer droplets and crosslinked microgels," *Sci. Adv.*, vol. 2, no. 10, Oct. 2016, Art. no. e1600964.
- [4] Y. Wang et al., "Nature-inspired micropatterns," *Nat. Rev. Methods Primers*, vol. 3, no. 1, p. 68, 2023.
- [5] Z. Liu, D. Sun, and C. Wang, "Evaluation of cell-cell interaction methods by integrating single-cell RNA sequencing data with spatial information," *Genome Biol.*, vol. 23, no. 1, pp. 1–38, 2022.
- [6] S. Takayama et al., "Patterning cells and their environments using multiple laminar fluid flows in capillary networks," *Proc. Nat. Acad. Sci.*, vol. 96, no. 10, pp. 5545–5548, May 1999.
- [7] Y. S. Chen et al., "Liver-lobule-mimicking patterning via dielectrophoresis and hydrogel photopolymerization," *Sens. Actuators B, Chem.*, vol. 343, Sep. 2021, Art. no. 130159.
- [8] N. Macdonald, A. Menachery, J. Reboud, and J. Cooper, "Creating tissue on chip constructs in microtire plates for drug discovery," *RSC Adv.*, vol. 8, no. 18, pp. 9603–9610, 2018.
- [9] C. Dai et al., "Robotic manipulation of deformable cells for orientation control," *IEEE Trans. Robot.*, vol. 36, no. 1, pp. 271–283, Feb. 2020.
- [10] J. Wang and Q. Zou, "Rapid probe engagement and withdrawal with force minimization in atomic force microscopy: A learning-based online-searching approach," *IEEE/ASME Trans. Mechatron.*, vol. 25, no. 2, pp. 581–593, Apr. 2020.
- [11] X. Hu et al., "On-chip hydrogel arrays individually encapsulating acoustic formed multicellular aggregates for high throughput drug testing," *Lab Chip*, vol. 20, no. 12, pp. 2228–2236, May 2020.
- [12] J. P. Armstrong et al., "Engineering anisotropic muscle tissue using acoustic cell patterning," *Adv. Mater.*, vol. 30, no. 43, Sep. 2018, Art. no. 1802649.
- [13] H. Zhou and G. Alici, "A magnetically actuated novel robotic capsule for site-specific drug delivery inside the gastrointestinal tract," *IEEE Trans. Syst. Man Cybern.*, vol. 52, no. 6, pp. 4010–4020, Jun. 2022.
- [14] X. Yang et al., "An agglutinate magnetic spray transforms inanimate objects into millirobots for biomedical applications," *Sci. Robot.*, vol. 5, no. 48, 2020, Art. no. eabc8191.
- [15] H. Wang et al., "Data-driven parallel adaptive control for magnetic helical microrobots with derivative structure in uncertain environments," *IEEE Trans. Syst. Man Cybern.*, vol. 54, no. 7, pp. 4139–4150, Jul. 2024.
- [16] T. Xu, C. Huang, Z. Lai, and X. Wu, "Independent control strategy of multiple magnetic flexible millirobots for position control and path following," *IEEE Trans. Robot.*, vol. 38, no. 5, pp. 2875–2887, Oct. 2022.
- [17] L. Sun et al., "Recent advances in microfluidic technologies for separation of biological cells," *Biomed. Microdevices*, vol. 22, no. 3, pp. 1–16, 2020.
- [18] Y. Zhang et al., "Detection and isolation of free cancer cells from ascites and peritoneal lavages using optically induced electrokinetics (OEK)," *Sci. Adv.*, vol. 6, no. 32, Aug. 2020, Art. no. eaba9628.
- [19] W. Liang et al., "A review on optoelectrokinetics-based manipulation and fabrication of micro/nanomaterials," *Micromachines*, vol. 11, no. 1, p. 78, Jan. 2020.
- [20] S. Zhang et al., "Optoelectronic tweezers: A versatile toolbox for nano-/micro-manipulation," *Chem. Soc. Rev.*, vol. 51, no. 22, pp. 9203–9242, Oct. 2022.
- [21] P. Y. Chiou, A. T. Ohta, and M. C. Wu, "Massively parallel manipulation of single cells and microparticles using optical images," *Nature*, vol. 436, no. 7049, pp. 370–372, Jul. 2005.
- [22] W. Liang, L. Liu, H. Zhang, Y. Wang, and W. J. Li, "Optoelectrokinetics-based microfluidic platform for bioapplications: A review of recent advances," *Biomicrofluidics*, vol. 13, no. 5, Sep. 2019, Art. no. 51502.
- [23] S. Liang et al., "Interaction between positive and negative dielectric microparticles/microorganism in optoelectronic tweezers," *Lab Chip*, vol. 21, no. 22, pp. 4379–4389, 2021.
- [24] T. K. Chiu et al., "Optically-induced-dielectrophoresis (ODEP)-based cell manipulation in a microfluidic system for high-purity isolation of integral circulating tumor cell (CTC) clusters based on their size characteristics," *Sens. Actuators B, Chem.*, vol. 258, pp. 1161–1173, Apr. 2018.
- [25] A. G. Banerjee, S. Chowdhury, W. Losert, and S. K. Gupta, "Real-time path planning for coordinated transport of multiple particles using optical tweezers," *IEEE Trans. Autom. Sci. Eng.*, vol. 9, no. 4, pp. 669–678, Oct. 2012.
- [26] J. Liu et al., "POMDP-based real-time path planning for manipulation of multiple microparticles via optoelectronic tweezers," *Cyborg Bionic Syst.*, vol. 2022, Nov. 2022, Art. no. 9890607.
- [27] L. Mennillo et al., "Adaptive autonomous navigation of multiple optoelectronic microrobots in dynamic environments," *IEEE Robot. Autom. Lett.*, vol. 7, no. 4, pp. 11102–11109, Oct. 2022.
- [28] S. Chowdhury et al., "Automated cell transport in optical tweezers-assisted microfluidic chambers," *IEEE Trans. Autom. Sci. Eng.*, vol. 10, no. 4, pp. 980–989, Oct. 2013.
- [29] X. Li, L. Gao, Q. Pan, L. Wan, and K.-M. Chao, "An effective hybrid genetic algorithm and variable neighborhood search for integrated process planning and scheduling in a packaging machine workshop," *IEEE Trans. Syst. Man Cybern.*, vol. 49, no. 10, pp. 1933–1945, Oct. 2019.
- [30] Y. Xu et al., "Path planning optimization with multiple pesticide and power loading bases using several unmanned aerial systems on segmented agricultural fields," *IEEE Trans. Syst. Man Cybern.*, vol. 53, no. 3, pp. 1882–1894, Mar. 2023.
- [31] D. Tian, H. Fang, Q. Yang, and Y. Wei, "Decentralized motion planning for multiagent collaboration under coupled LTL task specifications," *IEEE Trans. Syst. Man Cybern.*, vol. 52, no. 6, pp. 3602–3611, Jun. 2022.
- [32] S. H. Semnani, H. Liu, M. Everett, A. De Ruiter, and J. P. How, "Multi-agent motion planning for dense and dynamic environments via deep reinforcement learning," *IEEE Robot. Autom. Lett.*, vol. 5, no. 2, pp. 3221–3226, Apr. 2020.
- [33] Z. He, L. Dong, C. Sun, and J. Wang, "Asynchronous multithreading reinforcement-learning-based path planning and tracking for unmanned underwater vehicle," *IEEE Trans. Syst. Man Cybern.*, vol. 52, no. 5, pp. 2757–2769, May 2022.
- [34] Y. Yang, M. A. Bevan, and B. Li, "Hierarchical planning with deep reinforcement learning for 3D navigation of microrobots in blood vessels," *Adv. Intell. Syst.*, vol. 4, no. 11, Sep. 2022, Art. no. 2200168.
- [35] T. T. Nguyen, N. D. Nguyen, and S. Nahavandi, "Deep reinforcement learning for multiagent systems: A review of challenges, solutions, and applications," *IEEE Trans. Cybern.*, vol. 50, no. 9, pp. 3826–3839, Sep. 2020.
- [36] Z. Zhang, Y.-S. Ong, D. Wang, and B. Xue, "A collaborative multiagent reinforcement learning method based on policy gradient potential," *IEEE Trans. Cybern.*, vol. 51, no. 2, pp. 1015–1027, Feb. 2021.
- [37] G. Ji, Q. Gao, T. Zhang, L. Cao, and Z. Sun, "A heuristically accelerated reinforcement learning-based neurosurgical path planner," *Cyborg Bionic Syst.*, vol. 4, p. 26, May 2023.
- [38] Y. Gao et al., "Asymmetric self-play-enabled intelligent heterogeneous multirobot catching system using deep multiagent reinforcement learning," *IEEE Trans. Robot.*, vol. 39, no. 4, pp. 2603–2622, Aug. 2023, doi: [10.1109/TRO.2023.3257541](https://doi.org/10.1109/TRO.2023.3257541).

- [39] K. Wan, D. Wu, B. Li, X. Gao, Z. Hu, and D. Chen, "ME-MADDPG: An efficient learning-based motion planning method for multiple agents in complex environments," *Int. J. Intell. Syst.*, vol. 37, no. 3, pp. 2393–2427, Dec. 2022.
- [40] A. Macwan, J. Vilela, G. Nejat, and B. Benhabib, "A multirobot path-planning strategy for autonomous wilderness search and rescue," *IEEE Trans. Cybern.*, vol. 45, no. 9, pp. 1784–1797, Sep. 2015.
- [41] F. Ding et al., "Real-time trajectory planning and tracking control of bionic underwater robot in dynamic environment," *Cyborg Bionic Syst.*, vol. 5, p. 112, May 2024.
- [42] W. Liang, S. Wang, Z. Dong, G.-B. Lee, and W. J. Li, "Optical spectrum and electric field waveform dependent optically-induced dielectrophoretic (ODEP) micro-manipulation," *Micromachines*, vol. 3, no. 2, pp. 492–508, May 2012.
- [43] H. W. Kuhn, "The Hungarian method for the assignment problem," *Naval Res. Logist. Quart.*, vol. 2, nos. 1–2, pp. 83–97, 1955.
- [44] C.-L. Liu and T.-H. Huang, "Dynamic job-shop scheduling problems using graph neural network and deep reinforcement learning," *IEEE Trans. Syst. Man Cybern., Syst.*, vol. 53, no. 11, pp. 6836–6848, Nov. 2023.
- [45] Q. Li, W. Lin, Z. Liu, and A. Prorok, "Message-aware graph attention networks for large-scale multi-robot path planning," *IEEE Robot. Autom. Lett.*, vol. 6, no. 3, pp. 5533–5540, Jul. 2021.
- [46] J. Liu et al., "Dynamic control framework for automated particle transport based on optically induced dielectrophoresis," in *Proc. IEEE Int. Conf. Real-Time Comput. Robot. (RCAR)*, 2022, pp. 225–230.



Juan Cui received the Ph.D. degree in mechanical engineering from the Beijing Institute of Technology, Beijing, China, in 2020.

She is currently a postdoctoral student with Xi'an Jiaotong University, and also an Associate Professor with the North University of China, Taiyuan, China, since 2020. Her research interests are focused on micronano manipulation, biofabrication, and biosensor.



Hen-Wei Huang received the B.S. and M.S. degrees in mechanical engineering from National Taiwan University, Taipei, Taiwan, in 2011 and 2012, respectively, and the Ph.D. degree in robotics technology from ETH Zürich, Zürich, Switzerland, in 2018.

He is currently an Assistant Professor with Nanyang Technological University, Singapore. His research interests include in vivo wireless sensor networks, personalized medicine, controlled drug delivery, robotics, and translational medicine.



Qiang Huang (Fellow, IEEE) received the B.S. and M.S. degrees in electrical engineering from the Harbin Institute of Technology, Harbin, China, in 1986 and 1989, respectively, and the Ph.D. degree in mechanical engineering from Waseda University, Tokyo, Japan, in 1996. He

is currently a Professor and the Director of the Key Laboratory of Biomimetic Robots and Systems, Ministry of Education of China, and the Executive Director of Beijing Advanced Innovation Center for Intelligent Robots and Systems, and the Vice Director of the Key Laboratory of Intelligent Control and Decision of Complex System, Beijing Institute of Technology, Beijing, China.



Jiaxin Liu received the B.S. degree in mechanical engineering from Beijing Jiaotong University, Beijing, China, in 2020. He is currently pursuing the Ph.D. degree in mechanical engineering with the Beijing Institute of Technology, Beijing.

His research interest includes micro/nano manipulation and navigation control of micro/nano machines.



Shilong Qin received the B.S. degree in mechanical engineering from the University of Science and Technology Beijing, Beijing, China, in 2022. He is currently pursuing the master's degree in mechanical engineering with the Beijing Institute of Technology, Beijing.

His research interest includes micro/nano manipulation and algae research.



Toshio Fukuda (Life Fellow, IEEE) received the B.S. degree from Waseda University, Tokyo, Japan, in 1971, and the M.S. and Ph.D. degrees from the University of Tokyo, Tokyo, in 1973 and 1977, respectively.

He is currently a Professor with the Department of Micro-Nano Systems Engineering, Nagoya University, Nagoya, Japan, where he is mainly engaged with the research fields of intelligent robotic systems, cellular robotic systems, mechatronics, and micro/nano robotics. From 1977 to 1982, he was

with the National Mechanical Engineering Laboratory, Tsukuba, Japan. From 1982 to 1989, he was with the Science University of Tokyo, Tokyo. From 1989, he was with Nagoya University, where he was a Professor with the Department of Micro System Engineering and a Professor with Meijo University, Nagoya.



Qing Shi (Senior Member, IEEE) received the B.S. degree in mechatronics from the Beijing Institute of Technology, Beijing, China, in 2006, and the Ph.D. degree in biomedical engineering from Waseda University, Shinjuku, Japan, in 2012.

He was a Research Associate with GCOE, Global Robot Academia, Waseda University, from 2009 to 2013. He is currently a Professor with the School of Mechatronical Engineering, Beijing Institute of Technology. His research interests include bio-inspired robots, computer vision, and micro/nano robotics.



Huaping Wang (Member, IEEE) received the B.S. degree in mechatronics and the Ph.D. degree in mechanical engineering from the Beijing Institute of Technology, Beijing, China, in 2010 and 2015, respectively.

From 2012 to 2013, he was a Special Research Student with Nagoya University, Nagoya, Japan. Since July 2015, he has been an Assistant Professor with the Beijing Institute of Technology. His research interests include applications of micronano robotics and biomanipulation under micronano scale.